Acta Oceanol. Sin., 2023, Vol. 42, No. 2, P. 44–55
https://doi.org/10.1007/s13131-021-1976-y
http://www.aosocean.com
E-mail: ocean2@hyxb.org.cn

Vertical structure of tidal currents in the Xuliujing Section of Changjiang River Estuary

Zhigao Chen[1, 2, 3, 4*], Ya Ban[2], Xiaoye Chen[1], Dajun Li[1], Shengping Wang[1, 4*]

[1] Faculty of Geomatics, East China University of Technology, Nanchang 330013, China

[2] Chongqing Academy of Metrology and Quality Inspection, Chongqing 401120, China

[3] Nanjing White Shark Surveying and Mapping Technology Co., Ltd, Nanjing 210038, China

[4] Key Laboratory of Marine Environmental Survey Technology and Application, Ministry of Natural Resources, Guangzhou 510300, China

Received 26 June 2021; accepted 14 November 2021

Abstract

Three long-term fixed acoustic Doppler current profilers were first used for investigating the vertical structure of tidal currents in Xuliujing Section of Changjiang River Estuary. Moreover, three different periods (spring, summer and fall) were also considered for investigating seasonal variations. The semi-diurnal tides were the most energetic, with along-channel speed of up to 80 cm/s for M_2 constituent, which dominates at all stations with percent energy up to 65%–75% during seasons. The shape of tidal ellipses of the most energetic semi-diurnal constituent M_2 showed obvious polarization of the flow paralleling to the riverbank, with the minor semi-axis being generally less than 20% of the major one. The maximum velocity of mean current is appeared in top layers at all the three stations, and the velocity decreased with the depth. The seasonal variations of direction are also observed, which is probably caused by complex local topography since the erosion and deposition in riverbed. Observed vertical variation of four parameters of M_2 ellipses, agreed well with the optimally fit frictional solutions in top and middle layers. However, there was an obvious difference between frictional model and observed data in the lower water column. Discrepancies are probably on account of stratification, which strengthens in summer and fall due to the freshening influence of the Changjiang River Estuary outflow.

Key words: vertical structure, seasonal variations, tidal current, mean current, acoustic Doppler current profiler, Changjiang River Estuary

Citation: Chen Zhigao, Ban Ya, Chen Xiaoye, Li Dajun, Wang Shengping. 2023. Vertical structure of tidal currents in the Xuliujing Section of Changjiang River Estuary. Acta Oceanologica Sinica, 42(2): 44–55, doi: 10.1007/s13131-021-1976-y

1 Introduction

Flow in estuaries is very complex, characterized by the interactions of tidal currents, runoff (outflow), topography constraint and strong turbulence. Although the runoff or outflow may have large speed in tidal river, the weaker tidal currents are also important in determining the transport of dissolved and particulate matter in suspension (Bolaños et al., 2013; López et al., 2021). Knowledge of the vertical and horizontal structure of tidal currents is important to understand the dispersal and net drift of sediment and pollutants in the water column, and it is vital for long-term estuarine management (Prandle, 1982; Davies, 1990; Siagian et al., 2021).

Observations of basic tidal current structure have been carried out all over the world. The energy of tidal currents in coastal areas differs according to water depth and location and is driven by distinct responses to astronomical forcing (DiMarco and Reid, 1998; Tsimplis, 2000; Teague et al., 2002; Bi et al., 2019). Observation results usually indicate the current amplitude decrease toward the bottom of the water column and a phase advance with depth, indicating that the maximum current is reached earlier at depth than at the surface (Kundu et al., 1981; Tsimplis, 2000; Sánchez-Román et al., 2008). Analytic models for frictional bottom boundary layers have been developed to account for the observed amplitude decrease and phase advance. A constant eddy viscosity model is often used to compare with observations and the results showed that the model did well in describing most of the tidal current features throughout all depths (Kundu et al., 1981; Tsimplis, 2000; Codiga and Rear, 2004).

Changjiang River Estuary is the largest and most important estuary in China, which is world-famous for its great abundance and development intensity of soil and water, water transport and fishery resources. With an average annual discharge of 3.0×10^4 m^3/s, Changjiang River accounts for 90% of the total freshwater content into the East China Sea (Beardsley et al., 1985; Chen et al., 2001). Xuliujing Section located near Shanghai City, and it is about 110 km away from the river mouth (Fig. 1). Moreover,

Foundation item: The National Natural Science Foundation of China under contract Nos 41806114 and 42266006; the Jiangxi Provincial Natural Science Foundation under contract Nos 20202ACBL214019, 20181BAB216031 and 20212BBE53031; the Technological Innovation and Application Development in Chongqing under contract No. CSTB2022TIAD-GPX0016; the Incentive and Guidance Project of Scientific Research Performance for Scientific Research Institutes in Chongqing under contract No. cstc2021jxjl120017; the Open Fund of the Key Laboratory of Marine Environmental Survey Technology and Application of Ministry of Natural Resources under contract Nos MESTA-2020-A002 and MESTA-2021-B001.

*Corresponding author, E-mail: 531214372@qq.com; shpwang@ecut.edu.cn.

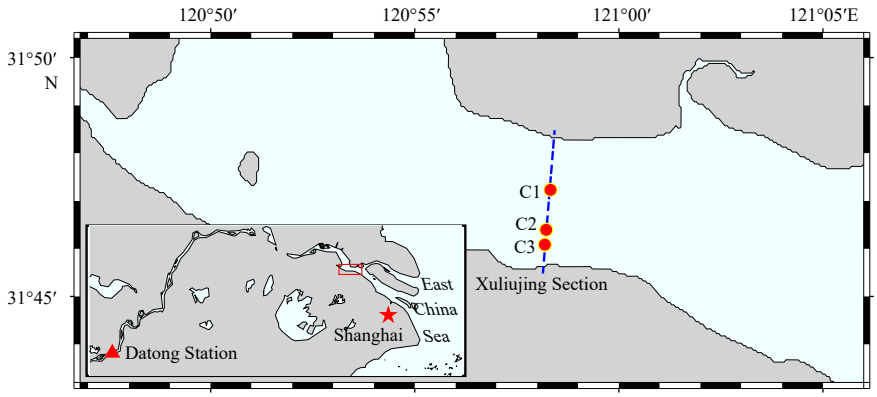

Fig. 1. Area of study. Red circles indicate the deploy location of the acoustic Doppler current profilers, and the dashed blue line represents Xuliujing Section.

Xuliujing is the demarcation point of South and North Branches and it is the starting point of multilevel branching in the Changjiang River Estuary. As an important boundary point for the Changjiang River to enter the estuary, the study of the tidal characteristics of Xuliujing becomes very important not only for the estuary scientific research itself, but also for the discussion of the impacts of major projects such as the Three Gorges Dam, the South-to-North Water Transfer Project, and the Changjiang River Estuary Deepwater Channel (Mei et al., 2019). Salinity intrusion generally reaches to less than 100 km seaward from the delta apex and can reach beyond the Xuliujing Section only during extremely low flows (Liu, 2004), so the studied area is generally subject to freshwater conditions.

Previous studies have resolved some of the major features of the tidal signal (Larsen et al., 1985; Yang et al., 2012). Nevertheless, as the measurement of these studies were taken by conventional current meters or the short-term data, the vertical resolution was poor. Three long-term mooring acoustic Doppler current profilers (ADCPs) are first used to investigate the vertical structure of the tidal currents in the Xuliujing Section of Changjiang River Estuary in this paper (Fig. 1). The contribution of primary tidal constituents is examined, as well as the structure of tidal currents in the horizontal and vertical primary. Influences of bathymetry variation on tidal current structure are also investigated.

The discharge of the Changjiang River is huge with which a marked seasonal variation (Fig. 2). The discharge is smaller in dry winter with the daily average is about 2.0×10^4 m^3/s and increases slightly in spring, while in the flood-period summer, the discharge reaches the peak of more than 5.0×10^4 m^3/s, which is more than twice that in winter. In fall, the discharge is decreasing. The seasons are therefore divided referring to the discharge variations. In this way, the mean currents at the study stations are also measured for interpreting variations of tidal currents during different seasons.

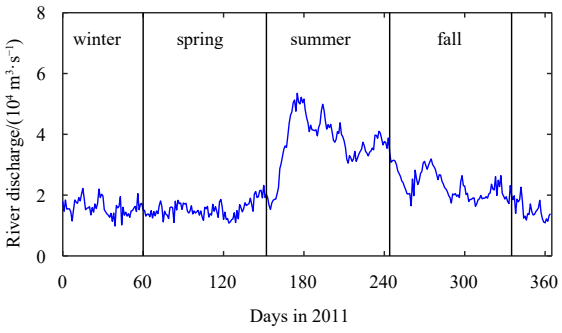

Fig. 2. Time series of the discharges at Datong Station (thumbnail image in Fig. 1) in 2011. Datong is the last permanent hydrometric station with long discharge records on the main Changjiang River, and the discharge is difficult to observe owing to the tidal influence. So the discharge in Datong is commonly regarded as the net discharge into the East China Sea.

2 Data and methods

Three 300 kHz Workhorse ADCPs, named C1, C2 and C3, were mounted upward on the river-bed at Xuliujing Section with different water depth (Fig. 3). C2 located in the thalweg of the river, while C1 and C3 located in northern and southern shallow water, respectively. The depth cell length was set as 1.0 m, and the sampling interval was set as 0.5 h for the three ADCP. The tidally-averaged depth, top and bottom unmeasured length, and number of valid bins for each ADCP profile were shown in the following Table 1. More details about the obtain and calibration of field data can be found in the literature of Zhao et al. (2016).

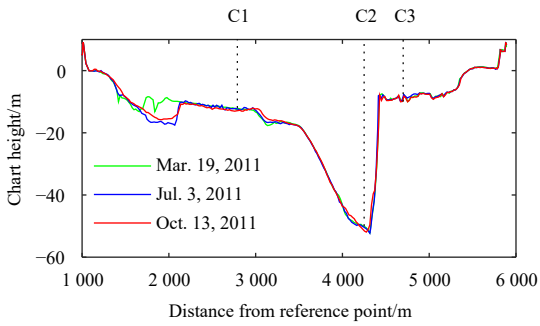

Fig. 3. Shapes of Xuliujing Section on three different dates of 2011. A boat-mounted single-beam echo sounder transducer (sonar) was used for bathymetric surveying at Xuliujing Section (Fig. 1) once a month. The echo sounder was a 208 kHz HY1600, 8 degree transducer, with a depth accuracy of 0.01 m+0.1%D (D is measured depth) and sampling rate of 5 Hz.

Table 1. Basic parameters of the three acoustic Doppler current profiler stations located in Xuliujing Section

Station	Depth/ m	Top unmeasured length/m	Bottom unmeasured length/m	Number of valid bins
C1	14.9	~2	~3	9
C2	51.5	~4	~4	45
C3	9.7	~2	~2	6

Three representative periods have been selected (March 1 to May 31, 2011, June 1 to August 31, 2011 and September 1 to November 30, 2011) for investigating seasonal variations of the vertical profiles according to the marked seasonal change of river discharge. Although these periods do not exactly correspond to specific seasons, they can also be referred as spring, summer and fall periods, respectively. All of the raw ADCP data are screened to exclude abnormal and poor data (Wong and Münchow, 1995). The screening criteria are set such that the valid ADCP data should meet the following requirements: error velocity is less than 6 cm/s, vertical velocity is less than 8 cm/s, and percentage good data is greater than 95%. Taking the result of traditional flowmeter as a reference, the ADCP velocity data achieved respectively 5 cm/s of measurement accuracies after the post-treatment.

Tidal constituents are analyzed by use of least squares harmonic method implemented by toolbox "T_tide" of Matlab (Pawlowicz et al., 2002). Velocity observations at each depth bin were used to compute the tidal ellipses of the main semidiurnal (M_2) and main diurnal (K_1) constituents. Tidal ellipses can be presented in terms of four parameters, including semi-major axis (W), semi-minor axis (w), orientation angle (Θ, direction of the maximum current speed), and the Greenwich phase lag (Φ). The conventional notations and basic equations are provided in Appendix A. Bootstrap method is used for estimating the standard error and 95% confidence intervals (Pawlowicz et al., 2002).

3 Results

3.1 *Energy partition*

Kinetic energy variance ratio (V_E) is usually used to examine the relative contribution of the tidal component to the total flow,

$$V_E = \left(\sigma^2_{\mathrm{KE_{fit}}} / \sigma^2_{\mathrm{KE_{dat}}}\right) \times 100\% \,. \tag{1}$$

V_E compares the kinetic energy variance σ^2_{KE}, where KE=$(u^2+v^2)/2$ is the kinetic energy per unit mass, of the multiple-constituent harmonics (subscript "fit") to that of the total measured raw velocities (subscript "dat"). Relative energy in individual tidal constituents is gauged as

$$E_n = \left(\mathrm{KE}_n \Big/ \sum_{i=1}^{N} \mathrm{KE}_i\right) \times 100\% \,, \tag{2}$$

where n is an index of the number (N) of constituents included in the harmonic fit. Five most energetic tidal constituents (including diurnal constituents O_1, K_1, and semidiurnal constituents N_2, M_2, and S_2, which are determined by harmonic analysis of 35 tidal constituents) are shown in the pie chart of Fig. 4. From the pie chart it appears that the total kinetic energy variance (area of the pie, including summed tidal and non-tidal variance) varies with season and water depth.

The general pattern is that the total kinetic energy variance decreases from the deep station (C2) to the shallow stations (C1 and C3). Total variances at the deep stations are obvious greater than that at shallow station. The relative contribution V_E ranges from 32% to 70%. At deeper station C2, V_E ranges from 36% to 70%, which is greater than that of shallower stations C1 (32%–52%) and C3 (34%–55%). The near-resonance of the trumpet-shaped Changjiang River Estuary to semidiurnal forcing may contribute to this energy distribution, which causes strongly amplified tidal currents to dominate the total kinetic energy near the mouth of Changjiang River relative to the far-field sites of East China Sea (Wang et al., 1999; Zhu et al., 2012). Similar patterns can also be found in other estuaries (Wünchow et al., 1992; Codiga and Rear, 2004).

In addition, percent energy (E_n) is used for accessing relative energy of individual tidal constituents to all the tidal components (histograms in Fig. 4). The M_2 constituent dominates at all stations with the E_n range from 65% to 75%. S_2 constituent is the next most important tide with the E_n range from 9% to 14%. For diurnal tidal constituents, the percent energy E_n of K_1 and O_1 is less than 5%. Overall, semi-diurnal tidal group is overwhelmingly dominant with the percent energy over 80%.

3.2 *Mean currents*

Frictional model using constant eddy viscosity may fail to capture the characteristics of observed tidal ellipses, especially for the bottom water layer. Therefore, the vertical structure of the mean currents (outflow) at three stations in different seasons is also examined for investigating the impact of outflow on tidal current (Fig. 5). The maximum flow velocity (speed) appears in top layers at all the three stations, and the velocity decreases with the depths slowly. In addition, for seasonal variations of mean currents is obvious: the velocity in summer with the maximum of 0.6 m/s is much bigger than that in another two seasons at each depth. The most important reason for this is that the annual discharge distribution of Changjiang River Basin directly controlled by the rainfall. Precipitation along the lower basin is primarily

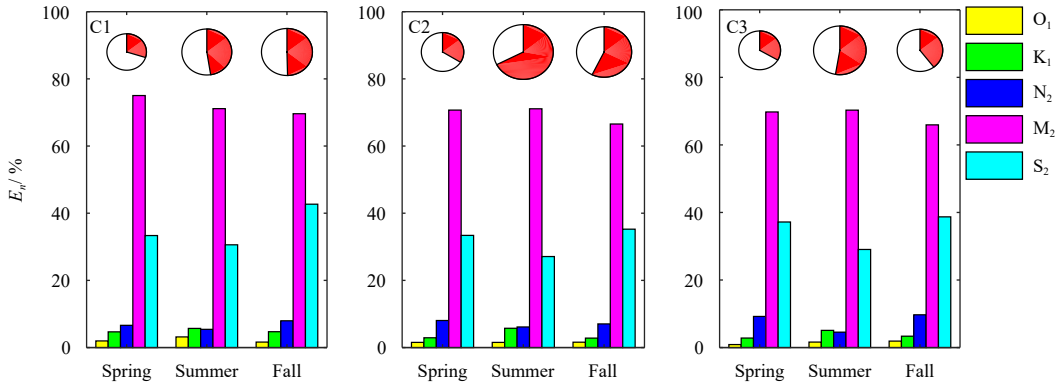

Fig. 4. Energy partition of vertical-averaged currents at three acoustic Doppler current profiler stations. Area of pie chart (top-row) indicates total kinetic energy variance $\sigma^2_{\mathrm{KE_{dat}}}$, and the sector is the Kinetic energy variance ratio V_E, which represents relative contribution of the tidal component to the total flow in each season. The largest pie appears at Station C2 in summer and it represents 0.67 $\mathrm{m^4/s^4}$. Histogram bars indicate percent energy E_n in the individual constituents.

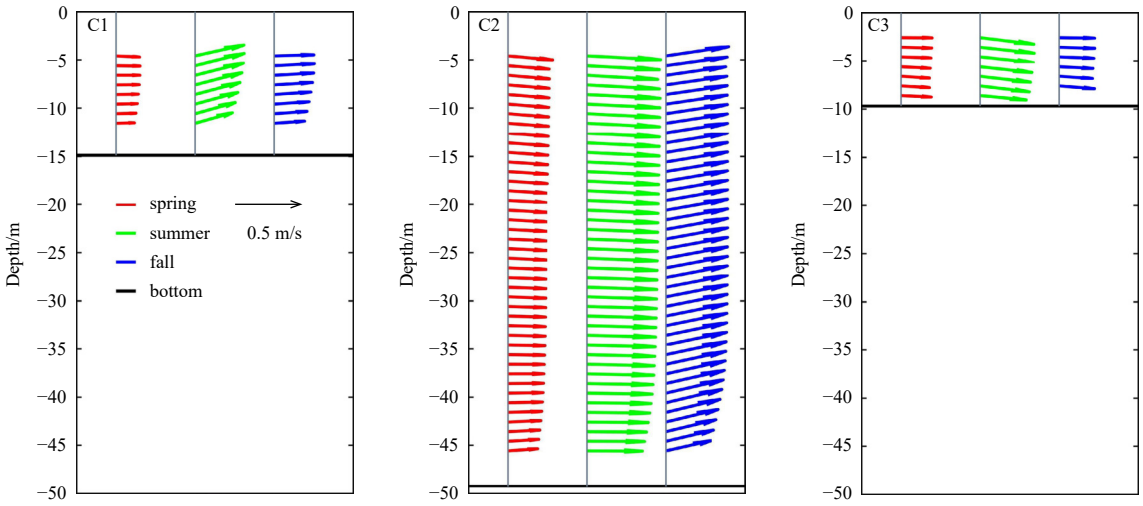

Fig. 5. Vertical profiles of mean current for the three acoustic Doppler current profiler stations. Direction is counterclockwise angle from east.

between May and August, account for nearly 73% of the annual total (Chen et al., 2001). The seasonal variations of mean currents are very consistent with discharge variations.

Flow direction remains almost constant from top to bottom water layers (within 10°) and parallel to the riverbank. The direction slowly increases with the depth until to the bottom in Station C1 and Station C2, on the contrary, it seems increases with the depth in Station C3. In addition, there have been some minor differences between directions of three seasons. These variations are probably due to complex local bathymetry since the erosion and deposition of riverbed significantly influence the depth of the three stations (Zhao et al., 2016). It is interesting to notice that Xuliujing Section locates in the middle of the bend river channel (Fig. 1). Influenced by both of Coriolis force and centrifugal force, the surface of the water appears transverse slope in which the water level of concave bank is higher than that of convex bank (Zhao et al., 2016). Therefore, the transverse shear velocity generated and will also result in the seasonal variations of direction. In addition, due to the freshwater condition, barotropic current dominated in all the three seasons (can be found in the following Section 3.3). The barotropic current varies with the seasons and it also contributes to the flow direction of main current.

3.3 *Tidal ellipses*

The vertical profiles of M_2 tidal ellipses at three stations in different seasons are displayed in Fig. 6, which shows the obvious polarization of the flow with the axis paralleling to the riverbank in all seasons. The minor semi-axis is always less than 20% of the major one, similar to the results in river mouth of Changjiang River Estuary (Pu et al., 2017), but significantly different from that in open-water estuary or shelf (Codiga and Rear, 2004; Herrera et al., 2008). The percentage of minor and major decreases towards the water surface.

Similarly, these diurnal ellipses align in almost the same direction and remain little changed at top and middle layers (not showed). The major semi-axis of K_1 less than one-fifth of that of M_2, which is highly consistent with the energy partition shown in Fig. 4. For this reason, the following harmonic analysis only be used to calculate the ellipse parameters of M_2 tidal constituent for investigating the vertical structure of observed and fitted tidal currents.

It is well known that the baroclinic effects play an important role in determining the currents structure in oceans and estuaries. Barotropic current and vertical distribution of baroclinic current for M_2 constituent at different stations are shown in Fig. 7. The top layer with an approximate thickness of 3 m in C1 station was slightly baroclinic. However, ADCPs are unable to accurately capture the complete velocity profile in open channels due to draft of ship and measurement errors near their transducers (Muste et al., 2010). In the experiments, the surface layer with an approximate thickness of 3 m of C1/C3 and 5 m of C2 is missing or contaminated and not showed in the figure. Therefore, the baroclinic effects are not well observed in the top layers. In addition, salinity intrusion generally reaches to less than 100 km seaward from the delta apex and can reach beyond the Xuliujing Section only during extremely low flows (Liu, 2004; Mei et al., 2019), so the studied area is generally subject to freshwater conditions. In this way, amplitudes of tidal constituents did not vary in depth for three stations, showing obvious barotropic behaviour.

3.4 *Harmonic analysis*

As showed in Fig. 8, the semi-major axis decreases slowly towards the bottom with the minimum value about 0.60 m/s, which indicates the speed of tidal current is becoming smaller. Unlike semi-major axis, the semi-minor axis is negative and very small whose values are all less than 0.05 m/s, which means that the tidal ellipse is nearly close to a straight line. Orientations remains almost constant in the vertical profiles of the three periods, which is consistent with the directions of mean current. It is worth noticing that the phases decrease toward the bottom, and the difference between that of upper and bottom is ~5°, which indicating upper currents lagging bottom currents about 10 min.

Only slight variations between the three seasons are found, one of them is that the phases in spring is slightly smaller than that of summer and fall. On the contrary, the semi-major axis of summer and fall are slightly bigger than that of spring.

Station C2 located in the thalweg of the river with the depth of 49.3 m. So, the vertical distribution in Station C2 has some similarities with that in Station C1, but it has its own characteristics: the semi-major axis almost remains constant in the upper profiles, and they decreases slowly from ~30 m towards the bottom. In addition, it is interesting to notice that the semi-minor axis is positive, which indicates the current vectors rotate counterclockwise around these ellipses. Discrepancies between different stations are probably due to high polarization of the flow paralleling

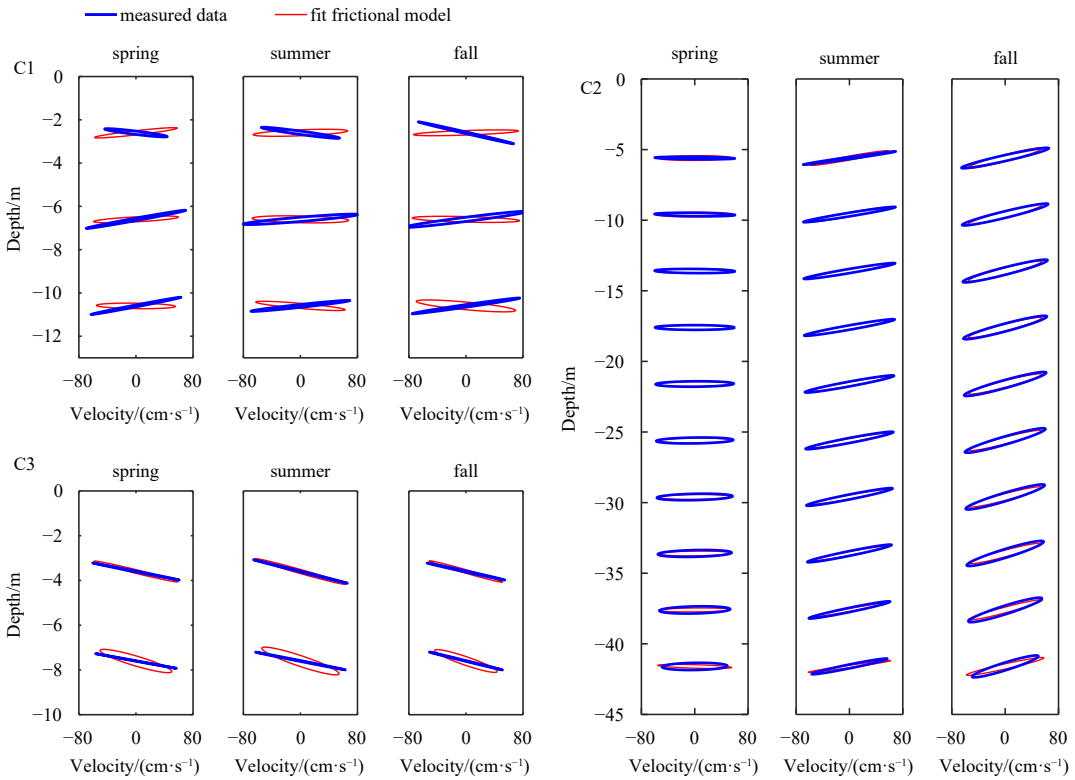

Fig. 6. M_2 tidal constituent ellipses at different depths. Blue lines indicate measured data, red lines are solution of optimally fit frictional model with a constant eddy viscosity and corresponding value of cost function (detailed in Section 4.1).

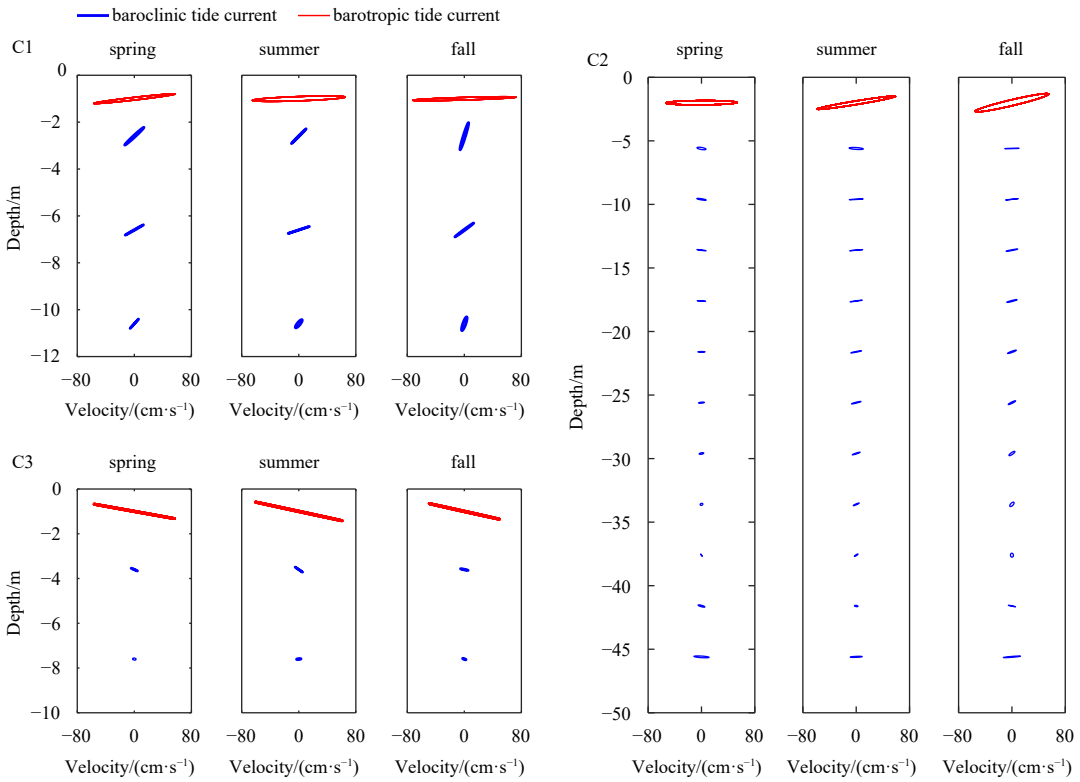

Fig. 7. Barotropic current (red line) and vertical distribution of baroclinic current (blue line) for M_2 constituent at different stations.

to the axis of the channel, and the semi-minor axis have little influence on the characters of the tidal currents.

Seasonal variations of orientations in Station C2 is similar to that of the directions of mean current, that the largest orientations is in fall, next is in summer, and the smallest is in spring. In addition, the phases in spring is slightly smaller than that of sum-

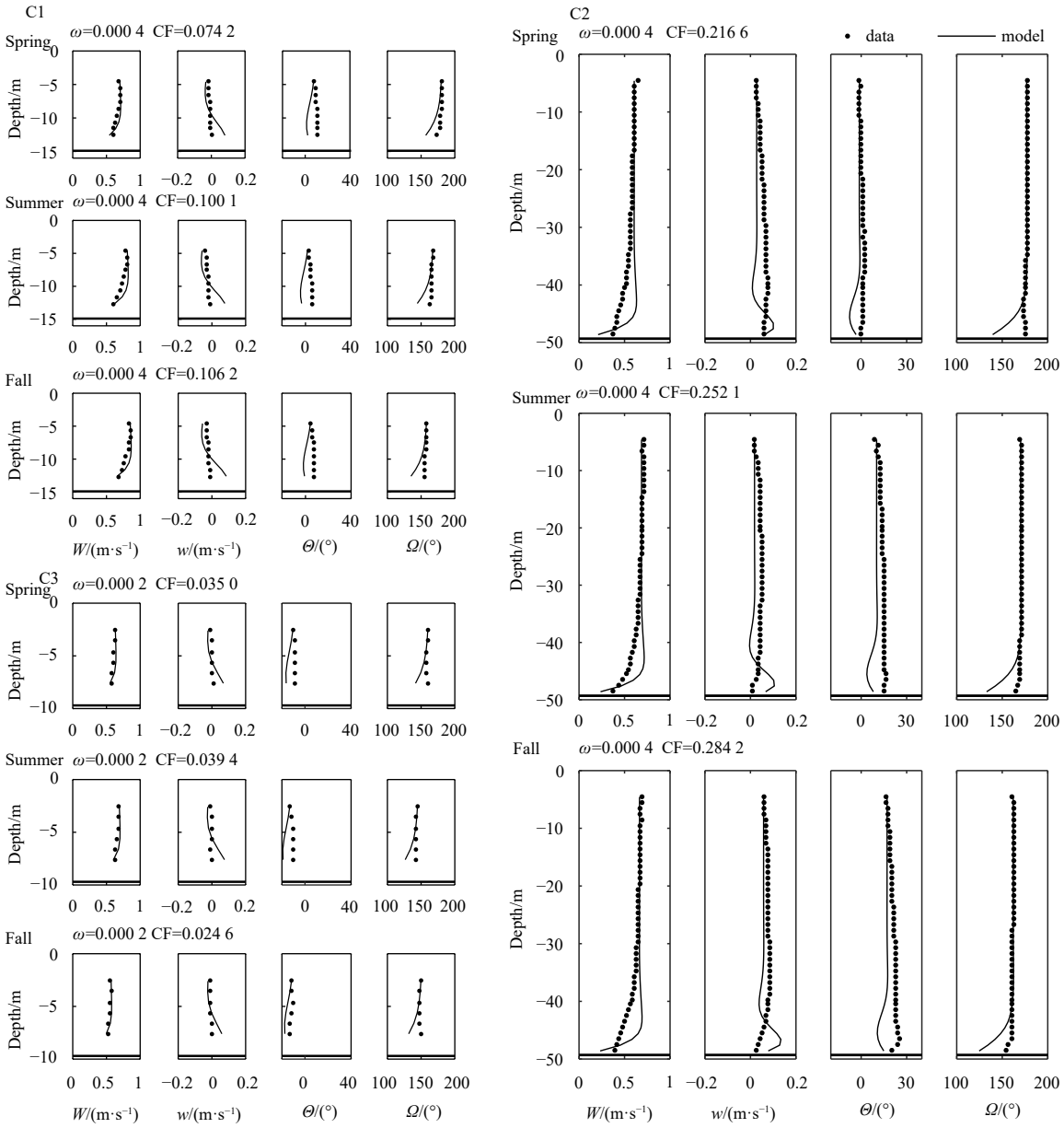

Fig. 8. The vertical distribution of M_2 ellipse parameters and the frictional model for three stations. Dots indicate measured data, solid lines are optimally fit model solution with a constant eddy viscosity and corresponding value of cost function (detailed in Section 4.1). Horizontal lines denote the tidal-averaged water depth.

mer and fall. On the contrary, the semi-major axes of summer and fall are slightly bigger than that of spring.

Because Stations C3 and C1 are both located in shallow water, the vertical distribution of the M_2 ellipses in Station C3 is very similar to that in Station C1. Only slightly difference is that the phases variation between upper and bottom is much smaller in the Station C3, where the maximum difference is ~3°.

4 Discussion

4.1 *Effects of bottom friction on variation of tidal ellipses*

The vertical variability of the tidal ellipse can be mainly attributed to the bottom friction, the contribution of the internal tides and the shear stresses variations from the adjacent layers (Tsimplis, 2000). This section will attempt to assess the effects of frictional variation contribution on the simple models.

Simple frictional models with a constant eddy viscosity have been shown capture characteristics of vertical structure reasonably well in some previous studies (Kundu et al., 1981; Tsimplis, 2000; Lee et al., 2011). Assuming the hydrostatic condition and an unstratified fluid, the horizontal pressure gradients are independent of water depth and are imposed by the free-surface height. A no-stress condition is applied to the surface and a no-slip condition is applied to the layer bottom. The solution of the model is deduced and provided in Appendix B. A cost function (CF) proposed by Codiga and Rear (2004) is used to realize optimal fitting between data and model velocity vectors,

$$\mathrm{CF}=\frac{1}{N}\sum_{i=1}^{N}\left(\left|\mathbf{w}_d^{+}(z_i)-\mathbf{w}_m^{+}(z_i)\right|^2+\left|\mathbf{w}_d^{-}(z_i)-\mathbf{w}_m^{-}(z_i)\right|^2\right), \quad (3)$$

where subscript d (m) indicates observed data (model solution), z is the height above the riverbed, i is the index of the N depth bins, $\mathbf{w}^+$ and $\mathbf{w}^-$ are respectively the first and second term of Eq. (A4) in Appendix A. The optimization is carried out using function ''fmincon'' and variants in Matlab, and achieve a minimum value of CF.

Optimal frictional model results (solid line) with the eddy viscosity (denoted as ω) are shown in Fig. 8 for three stations respectively. The optimally fit values of ω vary from 2×10^{-4} m^2/s to 8×10^{-4} m^2/s. The models are successful in describing some of the characteristics of the profiles of the M_2 constituent, especially in the top and middle layers, the frictional model is in good agreement with all observed characteristics. The model describes the semimajor axis decrease with depth, and the advance of the phase near the bottom in relation to the phase near the surface. It can be concluded that the indirect effect on the eddy viscosity is a main contributing factor, and the influences of bathymetric changes is secondary at these depths (Codiga and Rear, 2004).

Sample frictional models with constant eddy viscosity are successfully captured some ellipse characteristics at the middle and upper layers. Following will show that the models are failing to capture characteristics near the bottom.

4.2 *Inadequacies of frictional models*

The major disadvantage of the frictional model for all the three stations is in the lower water column. The observed low-depth semi-major axis is much smaller than that fit by frictional model. On the contrary, the phases fit by frictional model are much advanced than the observed ones. Therefore, frictional models using four different eddy viscosity ω are solved and shown in Fig. 9 to interpret the discrepancies. With the eddy viscosity increase, the semi-major axis is decreased correspondingly at deepest 10 m water column, but the variation gradient is much bigger than that of observation. In addition, it is noteworthy that the phases fit by frictional model decreases rapidly with the increasing eddy viscosity, while the observed phases only slightly decrease in the deepest 3–4 m water column.

Therefore, frictional model does not present a reasonable pattern with decreased or increased eddy viscosity values. The main reason is that the cost function shown in Eq. (3) weights equally for all depths so that changes occur in some lower layers have a limited impact on optimally fit. Complex topography and seasonal variations of estuarine outflow are contributed to this pattern (Mohn et al., 2013), but they are not considered at all in these frictional models.

4.3 *Influence of outflow on tidal current ellipses*

The characteristics of tidal ellipses cannot be captured well by eddy viscosity variation in astronomical forcing, which prompting other influencing factors may be investigated. Figures 10 and 11 show the mean current and M_2 ellipses at different depth for three seasons respectively. In each season, flow is generally eastward, that is from upstream to downstream. Peak speed of mean current reaches from 0.5 m/s to 0.7 m/s in summer for all stations. It is interesting to find that the orientations of ellipses are

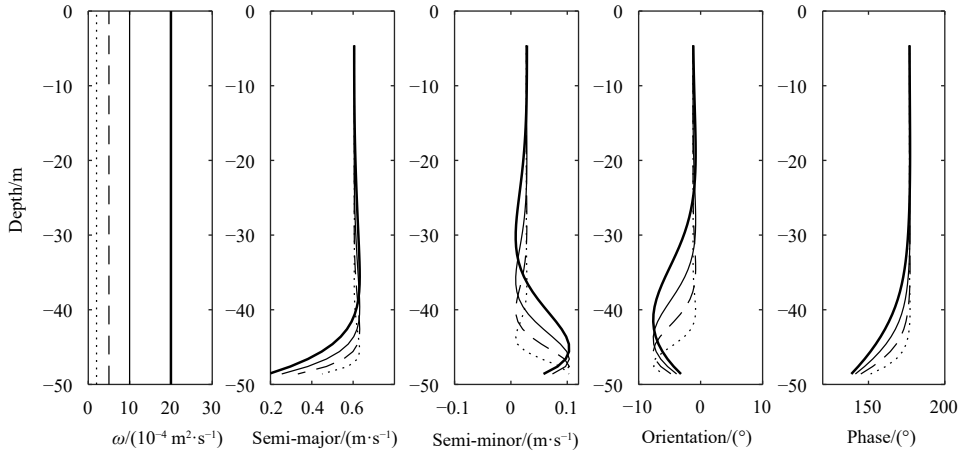

Fig. 9. Frictional model solutions using four different eddy viscosity ω appropriate to the Station C2 in spring. Dashed lines indicate ω=2×10^{-4} m^2/s, dots lines indicate ω=5×10^{-4} m^2/s, solid lines indicate ω=10×10^{-4} m^2/s, and thick solid lines indicate ω=20×10^{-4} m^2/s.

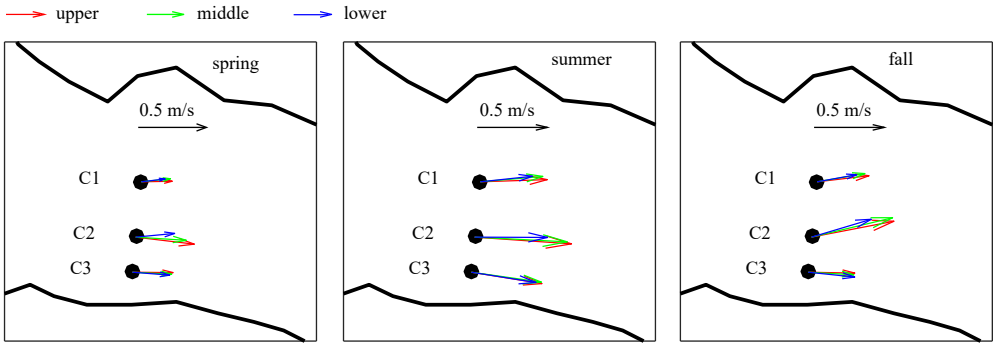

Fig. 10. Seasonal variation of mean currents at upper, middle and lower layers (0.2D, 0.5D and 0.8D, D is water depth) for three acoustic Doppler current profiler stations.

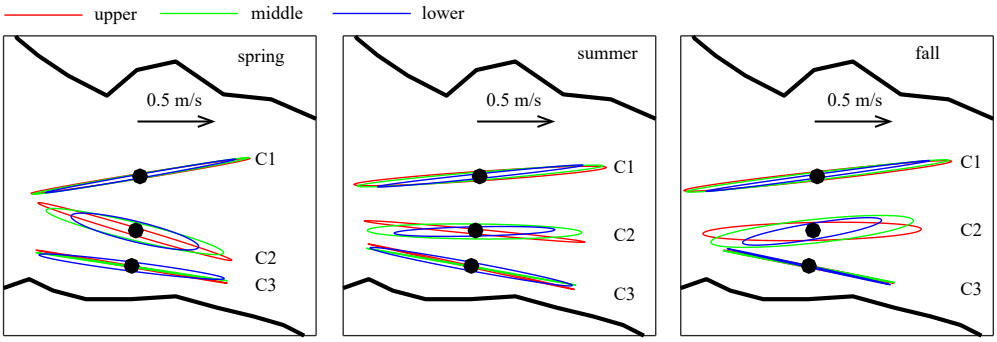

Fig. 11. Seasonal variation of M_2 ellipses at upper, middle and lower layers (0.2*D*, 0.5*D* and 0.8*D*, *D* is water depth) for three acoustic Doppler current profiler stations.

remarkably consistent with the directions of mean current in all seasons. This pattern is often caused by a combination of estuarine outflow and topography constraints, and it has qualitative characteristics for tidal ellipses.

In addition, the seasonal variations of semi-major axis are basically consistent with velocity of mean currents. Seasonal variations in tidal current ellipses may have relations with the seasonal cycle of stratification, which is enhanced significantly in summer and fall due to a combination of solar heating and the freshening induced by estuarine outflow (Ullman and Codiga, 2004). Lateral shear in the mean current can enhance or weaken effect of Coriolis parameter and thus shift the fixed tidal forcing frequency closer to or farther from resonance, thereby changing the response amplitude.

5 Conclusions

Three ADCPs mounted on the riverbed of Xuliujing Section are firstly used for investigating the vertical structure of the tidal currents and the seasonal variations in Changjiang River Estuary. The observations and analysis of the tidal current in this paper have revealed the noteworthy spatial variation of the tidal currents as well as some minor seasonal changes.

The M_2 constituent dominates at all stations with percent energy up to 65%–75% during seasons, while the sum percent energy of diurnal constituents account for less than 5%. The minor semi-axis is much less than the major one, which indicates that the shape of tidal ellipse is close to a straight line and parallel with the axis of the channel. This observation is similar to that in strait or gulf but significantly different from that in open-water estuary.

The maximum velocity of mean current appears in top layers at all the three stations, and the velocity decreases with the depth. Due to the seasonal variation of precipitation, the maximum velocity of 0.6 m/s in rainy season of summer is much bigger than that in spring and fall. Direction of mean current remain almost unchanged from the upper to the lower layers (within 10°) and parallel to the riverbank. The seasonal variations of direction are also observed, which is probably caused by complex local topography since the erosion and deposition in riverbed.

Due to the near-resonance of the trumpet-shaped Changjiang River Estuary to semidiurnal forcing, the semi-major axis of M_2 ellipse reaches the maximums ~0.80 m/s at the upper depth in study area, which is nearly twice as large as that in offshores. The orientations of ellipses are remarkably consistent with the directions of mean current in all seasons. The phases slowly decrease toward the bottom with the depth, and the difference between that of upper and bottom is ~5°, which indicating upper currents lagging bottom currents about 10 min.

Some of the characteristics of the profiles of the M_2 constituent are successfully described in the frictional model with a constant eddy viscosity, especially in the top and middle layers. However, the major inadequacies of the frictional model are in the lower water layers. Discrepancies are probably due to seasonal cycle in stratification, which is enhanced significantly in the summer and fall due to a combination of solar heating and the freshening influence of the estuarine outflow. In addition, lateral shear in the mean current can enhance or weaken effect of Coriolis parameter and change the response amplitude.

References

Beardsley R C, Limeburner R, Yu H, et al. 1985. Discharge of the Changjiang (Yangtze River) into the East China Sea. Continental Shelf Research, 4(1–2): 57–76, doi: 10.1016/0278-4343(85)90022-6

Bi Congcong, Bao Xianwen, Ding Yang, et al. 2019. Observed characteristics of tidal currents and mean flow in the northern Yellow Sea. Journal of Oceanology and Limnology, 37(2): 461–473, doi: 10.1007/s00343-019-8026-z

Bolaños R, Brown J M, Amoudry L O, et al. 2013. Tidal, riverine, and wind influences on the circulation of a macrotidal estuary. Journal of Physical Oceanography, 43(1): 29–50, doi: 10.1175/JPO-D-11-0156.1

Chen Zhongyuan, Li Jiufa, Shen Huanting, et al. 2001. Yangtze River of China: historical analysis of discharge variability and sediment flux. Geomorphology, 41(2–3): 77–91, doi: 10.1016/S0169-555X(01)00106-4

Codiga D L, Rear L V. 2004. Observed tidal currents outside Block Island Sound: offshore decay and effects of estuarine outflow. Journal of Geophysical Research, 109(C7): C07S05

Davies A G. 1990. A model of the vertical structure of the wave and current bottom boundary layer. In: Davies A M, ed. Modeling Marine Systems. Boca Raton: CRC Press, 263–297

DiMarco S F, Reid R O. 1998. Characterization of the principal tidal current constituents on the Texas-Louisiana shelf. Journal of Geophysical Research, 103(C2): 3093–3109, doi: 10.1029/97JC03289

Godin G. 1972. The Analysis of Tides. Toronto: University of Toronto Press

Herrera J L, Varela R A, Rosón G. 2008. Spatial variability of the barotropic M_2 constituent tidal current over the Rías Baixas Galician shelf (NW Spain). Journal of Marine Systems, 72(1–4): 189–199, doi: 10.1016/j.jmarsys.2007.07.006

Kundu P K, Blanton J O, Janopaul M M. 1981. Analysis of current observations on the Georgia shelf. Journal of Physical Oceanography, 11(8): 1139–1149, doi: 10.1175/1520-0485(1981)011<1139:AOCOOT>2.0.CO;2

Larsen L H, Cannon G A, Choi B H. 1985. East China Sea tide currents. Continental Shelf Research, 4(1–2): 77–103, doi: 10.1016/0278-4343(85)90023-8

Lee S, Lie H J, Cho C H, et al. 2011. Vertical structure of the M_2 tidal current in the Yellow Sea. Ocean Science Journal, 46(2): 73–84, doi: 10.1007/s12601-011-0007-x

Liu Dujuan. 2004. The situation and analysis of salinity intrusion in coastal areas, China. Journal of Geological Hazards and Environment Preservation, 15(1): 31–36

López M, Flores-Mateos L, Candela J. 2021. Tidal currents at the sills of the Northern Gulf of California. Continental Shelf Research, 227: 104513, doi: 10.1016/j.csr.2021.104513

Mei Xuefei, Zhang Min, Dai Zhijun, et al. 2019. Large addition of freshwater to the tidal reaches of the Yangtze (Changjiang) River. Estuaries and Coasts, 42(3): 629–640, doi: 10.1007/s12237-019-00518-0

Mohn C, Erofeeva S, Turnewitsch R, et al. 2013. Tidal and residual currents over abrupt deep-sea topography based on shipboard ADCP data and tidal model solutions for three popular bathymetry grids. Ocean Dynamics, 63(2–3): 195–208, doi: 10.1007/s10236-013-0597-1

Muste M, Kim D, González-Castro J A. 2010. Near-transducer errors in ADCP measurements: experimental findings. Journal of Hydraulic Engineering, 136(5): 275–289, doi: 10.1061/(ASCE)HY.1943-7900.0000173

Pawlowicz R, Beardsley B, Lentz S. 2002. Classical tidal harmonic analysis including error estimates in MATLAB using T_TIDE. Computers & Geosciences, 28(8): 929–937

Prandle D. 1982. The vertical structure of tidal currents and other oscillatory flows. Continental Shelf Research, 1(2): 191–207, doi: 10.1016/0278-4343(82)90004-8

Pu Xiang, Shi J Z, Hu Guodong. 2017. The effect of stratification on the vertical structure of the tidal ellipse in the Changjiang River Estuary, China. Journal of Hydro-environment Research, 15: 75–94, doi: 10.1016/j.jher.2017.03.004

Sánchez-Román A, Criado-Aldeanueva F, García-Lafuente J, et al. 2008. Vertical structure of tidal currents over Espartel and Camarinal sills, Strait of Gibraltar. Journal of Marine Systems, 74(1–2): 120–133, doi: 10.1016/j.jmarsys.2007.11.007

Siagian H, Ismanto A, Putra T W L, et al. 2021. Stratification on the vertical structure of the tidal ellipse and power density estimation in the Larantuka Strait, East Flores Based on ADCP measurement data. IOP Conference Series: Earth and Environmental Science, 750(1): 012023, doi: 10.1088/1755-1315/750/1/012023

Teague W J, Jacobs G A, Perkins H T, et al. 2002. Low-frequency current observations in the Korea/Tsushima Strait. Journal of Physical Oceanography, 32(6): 1621–1641, doi: 10.1175/1520-0485(2002)032<1621:LFCOIT>2.0.CO;2

Tsimplis M N. 2000. Vertical structure of tidal currents over the Camarinal Sill at the Strait of Gibraltar. Journal of Geophysical Research, 105(C8): 19709–19728, doi: 10.1029/2000JC900066

Ullman D S, Codiga D L. 2004. Seasonal variation of a coastal jet in the Long Island Sound outflow region based on HF radar and Doppler current observations. Journal of Geophysical Research, 109(C7): C07S06

Wang Kai, Fang Guohong, Feng Shizuo. 1999. A 3-D numerical simulation of M_2 tides and tidal currents in the Bohai Sea, the Huanghai Sea and the East China Sea. Haiyang Xuebao (in Chinese), 21(4): 1–13

Wong K C, Münchow A. 1995. Buoyancy forced interaction between estuary and inner shelf: observation. Continental Shelf Research, 15(1): 59–88, doi: 10.1016/0278-4343(94)P1813-Q

Wünchow A, Masse A K, Garvine R W. 1992. Astronomical and nonlinear tidal currents in a coupled estuary shelf system. Continental Shelf Research, 12(4): 471–498, doi: 10.1016/0278-4343(92)90087-Z

Yang Yunping, Li Yitian, Han Jianqiao, et al. 2012. Variation of tide limit and tidal current limit in Yangtze Estuary and its impact on projects. Journal of Sediment Research, 37(6): 46–51

Zhao Jianhu, Chen Zhigao, Zhang Hongmei, et al. 2016. Multiprofile discharge estimation in the tidal reach of Yangtze Estuary. Journal of Hydraulic Engineering, 142(12): 04016056, doi: 10.1061/(ASCE)HY.1943-7900.0001201

Zhu Xueming, Bao Xianwen, Song Dehai, et al. 2012. Numerical study on the tides and tidal currents in Bohai Sea, Yellow Sea and East China Sea. Oceanologia et Limnologia Sinica, 43(6): 1103–1113

Appendix A: Tidal current ellipses

Harmonics analysis of tidal currents is the extension of that for tides. The east (u) and north (v) component of a individual tidal constituent in time t including frequency σ, amplitudes (U and V), and phases (ξ and η), can be expressed as

$$\begin{cases} u = U\cos(\sigma t - \xi) \\ v = V\cos(\sigma t - \eta) \end{cases}. \tag{A1}$$

Introduces a complex velocity **w**,

$$\mathbf{w} = u + \mathrm{i}v, \tag{A2}$$

where the module and angle of **w** is the magnitude and direction of current and $\mathrm{i} = \sqrt{-1}$ is the imaginary unit. It can be obtained by Euler's formula

$$\begin{cases} \cos(\sigma t) = \dfrac{1}{2}\left(\mathrm{e}^{\mathrm{i}\sigma t} + \mathrm{e}^{-\mathrm{i}\sigma t}\right) \\ \sin(\sigma t) = \dfrac{1}{2\mathrm{i}}\left(\mathrm{e}^{\mathrm{i}\sigma t} - \mathrm{e}^{-\mathrm{i}\sigma t}\right) \end{cases}. \tag{A3}$$

Substitution of Eq. (1) into Eq. (2) and combined Eq. (3),

$$\mathbf{w} = \frac{1}{2}\begin{Bmatrix} [(U\cos\xi + V\sin\eta) + \mathrm{i}(V\cos\eta - U\sin\xi)]\,\mathrm{e}^{\mathrm{i}\sigma t} + \\ [(U\cos\xi - V\sin\eta) + \mathrm{i}(V\cos\eta + U\sin\xi)]\,\mathrm{e}^{-\mathrm{i}\sigma t} \end{Bmatrix}. \tag{A4}$$

Denoted

$$\begin{cases} \mathbf{a} = \dfrac{1}{2}(U\cos\xi + V\sin\eta) + \mathrm{i}(V\cos\eta - U\sin\xi) \\ \mathbf{b} = \dfrac{1}{2}(U\cos\xi - V\sin\eta) + \mathrm{i}(V\cos\eta + U\sin\xi) \end{cases}, \tag{A5}$$

then

$$\mathbf{w} = \mathbf{a}\mathrm{e}^{\mathrm{i}\sigma t} + \mathbf{b}\mathrm{e}^{-\mathrm{i}\sigma t}. \tag{A6}$$

Denote the first and second term of Eq. (A3) as complex $\mathbf{w}^+$ and $\mathbf{w}^-$, then the module and argument of $\mathbf{w}^+$ denote as A and α, and the module and argument of $\mathbf{w}^-$ denote as B and β,

$$\mathbf{w} = \mathbf{w}^+ + \mathbf{w}^- = \mathbf{a}\mathrm{e}^{\mathrm{i}\sigma t} + \mathbf{b}\mathrm{e}^{-\mathrm{i}\sigma t} = A\mathrm{e}^{\mathrm{i}(\sigma t+\alpha)} + B\mathrm{e}^{\mathrm{i}(-\sigma t+\beta)}, \tag{A7}$$

where the module of $\mathbf{w}^+$ is the constant A and arguments increase uniformly with time, which means that the movement track of $\mathbf{w}^+$ is a circle which rotates counter-clockwise (blue circle in Fig. A1). Similarly, the movement track of $\mathbf{w}^-$ is a circle which rotates clockwise (red circle in Fig. A1).

When t=0, $\mathbf{w}^+$=**a**=$A\mathrm{e}^{\mathrm{i}\alpha}$, $\mathbf{w}^-$=**b**=$B\mathrm{e}^{\mathrm{i}\beta}$, then **w** is the vector sum of **a** and **b** and marked in the t=0 in the ellipse of Fig. A1. $\mathbf{w}^+$ rotates counter-clockwise and $\mathbf{w}^-$ rotates clockwise with the same angular velocity, so the $\mathbf{w}^+$ and $\mathbf{w}^-$ meet at the angle Θ=(α+β)/2. Because the directions of $\mathbf{w}^+$ and $\mathbf{w}^-$ is the same at the angle Θ, so the module of **w** equal the sum of that of $\mathbf{w}^+$ and $\mathbf{w}^-$ and reaches the max value W=A+B, which is named semi-major axis. Similarly, semi-minor axis w=A–B is the min current velocity, and for positive values the tip of the velocity vector traces the ellipse in a counter-clockwise direction during the tidal period T, and vice versa. In addition, the angle between **a** and W named phase lag Φ=(β–α)/2, which means $\mathbf{w}^+$ rotates from **a** to W required time τ=(β–α)/2σ. From above, four parameters of tidal current ellipses can be expressed as following (Godin, 1972):

$$\begin{aligned} W &= A + B, & w &= A - B, \\ \Theta &= \frac{1}{2}(\alpha + \beta), & \Phi &= \frac{1}{2}(\beta - \alpha). \end{aligned} \tag{A8}$$

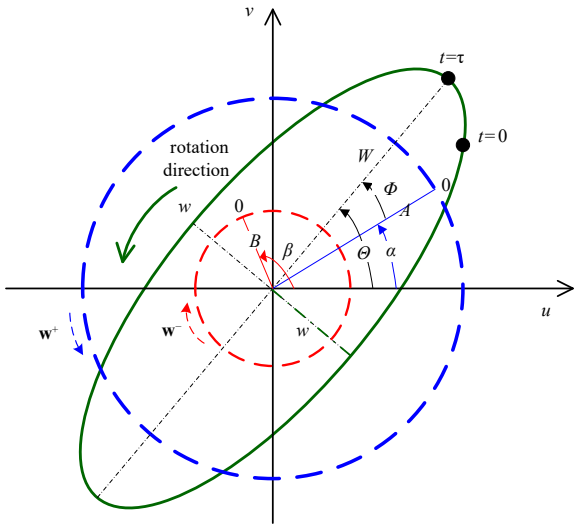

Fig. A1. Tidal current ellipse can be thought as the combination of two circles.

Appendix B: Solving the frictional models with constant eddy viscosity

Simple frictional models with a constant eddy viscosity capture characteristics of vertical structure reasonably well in some previous studies (Kundu et al., 1981; Tsimplis, 2000; Lee et al., 2011). The liner equations of motion can be expressed as

$$\begin{aligned}\frac{\partial u}{\partial t}-fv&=-\frac{1}{\rho_0}\frac{\partial p}{\partial x}+\frac{\partial}{\partial z}\left(\omega\frac{\partial u}{\partial z}\right)\\ \frac{\partial v}{\partial t}+fu&=-\frac{1}{\rho_0}\frac{\partial p}{\partial y}+\frac{\partial}{\partial z}\left(\omega\frac{\partial v}{\partial z}\right)\end{aligned}, \tag{B1}$$

where u and v are the east and north velocity components of the current, f is the Coriolis parameter and f=2εsinφ, ε is rotation angular velocity of the earth and φ is latitude, f=8.55×10^{-5} rad/s for Xuliujing Section; p is pressure, ρ_0 is density and ρ_0=1 for freshwater in Xuliujing Section, z is the height above the riverbed, and $\omega(z)$ is eddy viscosity at the height of z. A no-stress condition is applied at surface and a no-slip condition is applied at the layer bottom, the boundary conditions at the riverbed and surface are therefore

$$\begin{cases} u=v=0, & z=0,\\ \omega\dfrac{\partial u}{\partial z}=\omega\dfrac{\partial v}{\partial z}=0, & z=h,\end{cases} \tag{B2}$$

where positive value of z is upward and h is water depth. Introducing a complex numbers $\mathbf{G}$ to convert the two-dimensional vectors,

$$\mathbf{G}=-\frac{1}{\rho_0}\frac{\partial p}{\partial x}-\mathrm{i}\frac{1}{\rho_0}\frac{\partial p}{\partial y}\equiv\mathbf{c}\mathrm{e}^{\mathrm{i}\sigma t}+\mathbf{d}\mathrm{e}^{-\mathrm{i}\sigma t}. \tag{B3}$$

The second equation of the Eq. (B1) multiply the imaginary unit i, and plus the first Eq. of the Eq. (B1), With Eq. (B3) the Eq. (B1) becomes

$$\frac{\partial \mathbf{w}}{\partial t}+if\mathbf{w}-\omega\frac{\partial^2\mathbf{w}}{\partial z^2}=\mathbf{G}. \tag{B4}$$

Then put the Eq. (A6) $\mathbf{w}=\mathbf{a}\mathrm{e}^{\mathrm{i}\sigma t}+\mathbf{b}\mathrm{e}^{-\mathrm{i}\sigma t}$ into Eq. (B4):

$$\mathrm{i}\sigma\mathbf{a}\mathrm{e}^{\mathrm{i}\sigma t}-\mathrm{i}\sigma\mathbf{b}\mathrm{e}^{-\mathrm{i}\sigma t}+\mathrm{i}f\left(\mathbf{a}\mathrm{e}^{\mathrm{i}\sigma t}+\mathbf{b}\mathrm{e}^{-\mathrm{i}\sigma t}\right)-\left(\omega\frac{\mathrm{d}^2\mathbf{a}}{\mathrm{d}z^2}\mathrm{e}^{\mathrm{i}\sigma t}+\omega\frac{\mathrm{d}^2\mathbf{b}}{\mathrm{d}z^2}\mathrm{e}^{-\mathrm{i}\sigma t}\right)=\mathbf{c}\mathrm{e}^{\mathrm{i}\sigma t}+\mathbf{d}\mathrm{e}^{-\mathrm{i}\sigma t}. \tag{B5}$$

The coefficients of $\mathrm{e}^{\mathrm{i}\sigma t}$ and $\mathrm{e}^{-\mathrm{i}\sigma t}$ in both sides of Eq. (B5) should be equal, then

$$\begin{cases}\mathrm{i}\left(\sigma+f\right)\mathbf{a}-\omega\dfrac{\mathrm{d}^2\mathbf{a}}{\mathrm{d}z^2}=\mathbf{c}\\ \mathrm{i}\left(-\sigma+f\right)\mathbf{b}-\omega\dfrac{\mathrm{d}^2\mathbf{b}}{\mathrm{d}z^2}=\mathbf{d}\end{cases}. \tag{B6}$$

Eq. (B3) can also be expressed as:

$$\begin{cases} \dfrac{\mathrm{d}^2\mathbf{a}}{\mathrm{d}z^2} - \mathrm{i}\dfrac{(\sigma+f)}{\omega}\mathbf{a} = -\dfrac{\mathbf{c}}{\omega} \\ \dfrac{\mathrm{d}^2\mathbf{b}}{\mathrm{d}z^2} - \mathrm{i}\dfrac{(-\sigma+f)}{\omega}\mathbf{b} = -\dfrac{\mathbf{d}}{\omega} \end{cases}. \tag{B7}$$

Substitution of Eq. (A3) into Eq. (A7) produces, the boundary conditions can be expressed as:

$$\begin{cases} \mathbf{a} = \mathbf{b} = 0, & z = 0, \\ \dfrac{\mathrm{d}\mathbf{a}}{\mathrm{d}z} = \dfrac{\mathrm{d}\mathbf{b}}{\mathrm{d}z} = 0, & z = h. \end{cases} \tag{B8}$$

Solving this system of inhomogeneous second-order differential equation, that **a** and **b** can be written as functions of z. The finite depth solution of Eq. (B7) can be expressed as ratio of frictional current to frictionless current,

$$\begin{cases} \dfrac{\mathbf{a}}{\mathbf{a}_g} = 1 - \dfrac{\mathrm{e}^{\lambda_a(1+\mathrm{i})z} + \mathrm{e}^{2\lambda_a(1+\mathrm{i})h}\cdot\mathrm{e}^{-\lambda_a(1+\mathrm{i})z}}{1+\mathrm{e}^{2\lambda_a(1+\mathrm{i})h}} \\ \begin{cases} \dfrac{\mathbf{b}}{\mathbf{b}_g} = 1 - \dfrac{\mathrm{e}^{\lambda_b(1+\mathrm{i})z} + \mathrm{e}^{2\lambda_b(1+\mathrm{i})h}\cdot\mathrm{e}^{-\lambda_b(1+\mathrm{i})z}}{1+\mathrm{e}^{2\lambda_b(1+\mathrm{i})h}}, & \sigma < f \\ \dfrac{\mathbf{b}}{\mathbf{b}_g} = 1 - \dfrac{\mathrm{e}^{\lambda_b(1-\mathrm{i})z} + \mathrm{e}^{2\lambda_b(1-\mathrm{i})h}\cdot\mathrm{e}^{-\lambda_b(1-\mathrm{i})z}}{1+\mathrm{e}^{2\lambda_b(1-\mathrm{i})h}}, & \sigma > f \\ \dfrac{\mathbf{b}}{\mathbf{d}} = \dfrac{1}{\omega}z\left(h - \dfrac{z}{2}\right), & \sigma = f \end{cases} \end{cases}, \tag{B9}$$

where the subscript g in $\mathbf{a}_\mathrm{g}$ and $\mathbf{b}_\mathrm{g}$ means the frictionless current, and

$$\lambda_a = \sqrt{\frac{|\sigma+f|}{2\omega}}, \quad \lambda_b = \sqrt{\frac{|\sigma-f|}{2\omega}}. \tag{B10}$$